

# Angular momentum evolution of bulge stars in disc galaxies in NIHAO

Liang Wang,<sup>1</sup>★ Danail Obreschkow<sup>1b</sup>,<sup>1</sup> Claudia del P. Lagos<sup>1b</sup>,<sup>1,2</sup> Sarah M. Sweet<sup>1b</sup>,<sup>3</sup> Deanne Fisher<sup>1b</sup>,<sup>3</sup> Karl Glazebrook,<sup>3</sup> Andrea V. Macciò<sup>1b</sup>,<sup>4,5</sup> Aaron A. Dutton<sup>1b</sup><sup>4</sup> and Xi Kang<sup>6</sup>

<sup>1</sup>International Centre for Radio Astronomy Research (ICRAR), M468, University of Western Australia, 35 Stirling Hwy, Crawley, WA 6009, Australia

<sup>2</sup>ARC Centre of Excellence for All Sky Astrophysics in 3 Dimensions (ASTRO 3D)

<sup>3</sup>Centre for Astrophysics and Supercomputing, Swinburne University of Technology, PO Box 218, Hawthorn, VIC 3122, Australia

<sup>4</sup>New York University Abu Dhabi, PO Box 129188, Saadiyat Island, Abu Dhabi, United Arab Emirates

<sup>5</sup>Max-Planck-Institut für Astronomie, Königstuhl 17, D-69117 Heidelberg, Germany

<sup>6</sup>Purple Mountain Observatory, the Partner Group of MPI für Astronomie, 2 West Beijing Road, Nanjing 210008, China

Accepted 2018 November 2. Received 2018 November 2; in original form 2018 July 24

## ABSTRACT

We study the origin of bulge stars and their angular momentum (AM) evolution in 10 spiral galaxies with baryonic masses above  $10^{10} M_{\odot}$  in the Numerical Investigation of a Hundred Astrophysical Objects galaxy formation simulations. The simulated galaxies are in good agreement with observations of the relation between the specific AM and mass of the baryonic component and the stellar bulge-to-total ratio ( $B/T$ ). We divide the star particles at  $z = 0$  into disc and bulge components using a hybrid photometric/kinematic decomposition method that identifies all the central mass above an exponential disc profile as the ‘bulge’. By tracking the bulge star particles back in time, we find that on average 95 per cent of the bulge stars formed *in situ*, 3 per cent formed *ex situ* in satellites of the same halo, and only 2 per cent formed *ex situ* in external galaxies. The evolution of the AM distribution of the bulge stars paints an interesting picture: The higher the final  $B/T$ , the more the specific AM remains preserved during the bulge formation. In all cases, bulge stars migrate significantly towards the central region, reducing their average galactocentric radius by roughly a factor 2, independently of the final  $B/T$  value. However, in the higher  $B/T$  ( $\gtrsim 0.2$ ) objects, the velocity of the bulge stars increases and the AM of the bulge is almost conserved, whereas at lower  $B/T$  values, the velocity of the bulge stars decreases and the AM of the bulge reduces. The correlation between the evolution of the AM and  $B/T$  suggests that bulge formation and disc formation are closely linked and cannot be treated as independent processes.

**Key words:** methods: numerical – galaxies: bulges – galaxies: evolution – galaxies: formation – galaxies: kinematics and dynamics – galaxies: spiral.

## 1 INTRODUCTION

Angular momentum (AM)  $J$  has long been recognized as a fundamental quantity in galaxy formation and evolution. It is often convenient and physically meaningful to remove the implicit mass scaling of  $J$  by adopting the specific AM  $j \equiv J/M$ . The standard picture of cosmic structure formation predicts that dark matter (DM) and baryonic gas acquire similar specific AM via tidal torques from neighbouring structures. In the simple model, where the gas cools radiatively and settles in a spinning disc, the size of this disc is proportional to its  $j$  (Fall & Efstathiou 1980), whereas the size of the DM halo is independent of the AM.

Empirically, the global morphology of galaxies, as quantified by Hubble’s classical tuning fork, correlates strongly with specific AM. In fact, early-type and late-type galaxies at redshift  $z = 0$  obey similar scaling relations between stellar specific AM  $j_{\star}$  and mass  $M_{\star}$ , of the form  $j_{\star} \propto M_{\star}^{\alpha}$  with  $\alpha \sim 2/3$  (Fall 1983; Romanowsky & Fall 2012; Fall & Romanowsky 2013; Obreschkow & Glazebrook 2014; Cortese, Fogarty & Bekki 2016). However, these relationships are offset by about a factor  $\sim 5$  in  $j_{\star}$ , with early types having less AM. Obreschkow & Glazebrook (2014) refine this picture by using high-precision AM data from the THINGS survey and optical  $K$ -band bulge-to-total ratios ( $B/T$ ). In a sample with  $0 < B/T \lesssim 0.3$  and baryon mass  $M_b$  (stellar and cold gas mass) in the range  $10^9 M_{\odot} < M_b < 10^{11} M_{\odot}$ , they find a very strong correlation between  $M_b$ , the baryon specific AM  $j_b$ , and  $B/T$ .

It is a pressing theoretical challenge to explain how this observed relationship between morphology and AM arises in regular

\* E-mail: liang.wang@uwa.edu.au

galaxies. This work aims to shine a light on this discussion by tackling the time evolution of the bulge stars in regular star-forming disc galaxies in a cosmological smoothed-particle hydrodynamic (SPH) simulation. Naturally, this goal requires a clear definition of the ‘bulge’, not just in terms of its global mass and extent, but also in terms of identifying all star particles of the bulge so that they can be traced back in time. Observations regularly use photometric bulge–disc decomposition methods, relying on surface density (defining the bulge as a central overdensity) and/or colour (defining the bulge as the old central population). In turn, simulations often employ kinematic approaches (defining the bulge as the low-AM component; e.g. Obreja, Stinson & Dutton 2016). These definitions result in different bulge mass fractions and, more importantly, in a very different set of stars being labelled as bulge stars. To do justice to this complexity, we first carry out a detailed comparison of photometric and kinematic bulge–disc decompositions (Section 2) and then pick the definition most adequate to the *particular* set of questions addressed in this work.

Cosmological hydrodynamic simulations of galaxies from disc-dominated to bulge-dominated objects compare the simulation results with observations by considering the Tully–Fisher relation (Robertson et al. 2004; Governato, Willman & Mayer 2007; Stinson, Bailin & Couchman 2010; Piontek & Steinmetz 2011; Dutton, Obreja & Wang 2017), the AM content (Scannapieco et al. 2009), and the disc sizes (Brook, Governato & Roškar 2011). However, the simulated galaxies of early studies always had an unrealistic massive and concentrated bulge to the corresponding observed bulge (Binney, Gerhard & Silk 2001; Bullock, Dekel & Kolatt 2001; van den Bosch 2001; van den Bosch, Abel & Rupert 2002; D’Onghia et al. 2006; D’Onghia & Navarro 2007; Stinson et al. 2010; Scannapieco, Wadepuhl & Parry 2012). The failure of reproducing realistic disc galaxies with small bulges came from the fact that these simulations were plagued by overcooling and AM losses, resulting in compact, bulge-dominated galaxies.

In the past years, cosmological simulations have reached enough resolution to resolve bulges and included more realistic models for star formation and stellar feedback. These improvements have made it possible to produce realistic galactic discs (Agertz, Teyssier & Moore 2011; Guedes et al. 2011; Aumer, White & Naab 2013; Stinson, Bovy & Rix 2013b; Marinacci, Pakmor & Springel 2014; Roškar, Teyssier & Agertz 2014; Murante, Monaco & Borgani 2015; Colín et al. 2016; Grand, Gómez & Marinacci 2017). The most recent generation of large-volume hydrodynamical simulations of galaxy formation (e.g. Vogelsberger, Genel & Springel 2014; Schaye, Crain & Bower 2015) have managed to reproduce observed galaxies from the disc-dominated sequence and the bulge-dominated sequence (Genel, Fall & Hernquist 2015; Teklu, Remus & Dolag 2015; Zavala, Frenk & Bower 2016; DeFelippis et al. 2017; Lagos, Theuns & Stevens 2017a; Sokolowska, Capelo & Fall 2017).

In the conventional view, bulge stars have two main origins: galaxy–galaxy mergers and *in situ* formation in galactic discs. The former tend to result in pressure-supported, ‘classical’ bulges (Davies & Illingworth 1983), while the latter give rise to rotation-supported ‘pseudo’-bulges (Kormendy & Kennicutt 2004). D’Onghia & Navarro (2007) show that cooling in the highly dense inner region and dynamical friction of satellite galaxies dissipate the AM of gas, which results in compact discs. In contrast, Springel & Hernquist (2005) and Robertson, Bullock & Cox (2006) show that in idealized merger simulations with strong stellar feedback it is possible to form a disc-dominated galaxy if the initial disc is gas rich. Recent cosmological simulations also confirm that strong stel-

lar feedback is able to reduce the bulge mass and results in disc-dominated galaxies (Governato et al. 2007; Guedes et al. 2011; Brook, Stinson & Gibson 2012; Martig, Bournaud & Croton 2012; Stinson, Brook & Macciò 2013a; Christensen et al. 2014; Kannan, Stinson & Macciò 2014; Marinacci et al. 2014). Furthermore, Hopkins et al. (2009) and Kannan, Macciò & Fontanot (2015) suggest that mergers are not as efficient as previously thought in transforming discs into bulges and bulge formation depends on the gas disc fraction. Lagos, Stevens & Bower (2018a) using the EAGLE simulations divided mergers into dry (gas poor) and wet (gas rich), major/minor and analysed different spin alignments and orbital parameters. They found that mergers’ influence on the galaxy spin can be quite varied, and in the case of gas-rich mergers, galaxies can spin up significantly, while dry mergers tend to spin galaxies down. Therefore, the bulge formation couples with complex and only partially understood small-scale processes.

In this paper, we examine the origin and AM evolution of bulge stars in a subset of 10 spiral galaxies from the Numerical Investigation of a Hundred Astrophysical Objects (NIHAO; Wang, Dutton & Stinson 2015) project. All these bulges have pseudo-bulge properties. The NIHAO simulations are a suite of 88 hydrodynamical cosmological zoom-in simulations implementing the tree-smoothed particle hydrodynamics GASOLINE. The simulated galaxies cover a range in mass from  $10^5 \lesssim M_*/M_\odot \lesssim 10^{11}$ . The prescription for star formation and stellar feedback was developed in the Making Galaxies in a Cosmological Context (MAGICC; Stinson et al. 2013a) project. The NIHAO runs keep the same stellar physics at all scales. The stellar mass of each halo in the NIHAO sample agrees with the prediction from abundance matching (Wang et al. 2015). The galaxies in the NIHAO sample reproduce several observational results, such as the star formation main sequence (Wang et al. 2015), the column density profile of cool H I (Gutcke, Stinson & Macciò 2017), and the Tully–Fisher relation (Dutton et al. 2017). Given its high mass resolution, this sample allows us to track the evolution of the AM of bulge star particles and witness the formation of a bulge in a realistic cosmological environment.

This paper is organized as follows: In Section 2, we give an overview of the cosmological hydrodynamical simulations and the post-processing applied in this work. In Section 3, we study the origin of bulge stars and discuss the evolution of their AM, locations, and velocities. Section 4 discusses the coherent picture of how the bulges of galaxies form. Finally, in Section 5 we discuss and summarize our conclusions.

## 2 SIMULATIONS

The simulations we analyse in this work are a subsample of the NIHAO suite (Wang et al. 2015), based on an updated version of the MAGICC project (Stinson et al. 2013a). The NIHAO simulation suite is an unbiased sample of isolated haloes of present-day masses between  $M_{\text{halo}} \sim 4 \times 10^9 M_\odot$  and  $M_{\text{halo}} \sim 4 \times 10^{12} M_\odot$ . The initial conditions are created so that we typically have a million DM particles inside the virial radius of the target halo at redshift  $z = 0$ , across the whole mass range. We adopted the latest compilation of cosmological parameters from the *Planck* satellite (Planck Collaboration XVI 2014). DM particle masses range from  $\sim 10^4 M_\odot$  in our lowest mass haloes to  $\sim 10^6 M_\odot$  in our most massive haloes, and their force softenings range from  $\sim 150$  pc to  $\sim 900$  pc, respectively. Gas particles are less massive by factor of  $(\Omega_{\text{DM}}/\Omega_{\text{b}}) \simeq 5.48$ , and the corresponding force softenings are 2.34 times smaller. A comparison with other state-of-the-art simulations can be found in fig. 2 in Wang et al. (2015). More information on the collisionless

parent simulations, the force softening, and particle masses for the highest refinement level for each simulation and sample selection can be found in Dutton & Macciò (2014) and Wang et al. (2015).

We use the SPH code GASOLINE (Wadsley, Stadel & Quinn 2004), with a revised treatment of hydrodynamics as described in Keller et al. (2014). The code includes a subgrid model for turbulent mixing of metal and energy (Wadsley, Veeravalli & Couchman 2008), heating and cooling including photoelectric heating of dust grains, ultraviolet (UV) heating and ionization, and cooling due to hydrogen, helium, and metals (Shen, Wadsley & Stinson 2010).

## 2.1 Star formation and feedback

The star formation and feedback modelling follow what was used in the MAGICC simulations (Stinson et al. 2013a). The star formation recipe adopts a Kennicutt–Schmidt relation, where the star-forming gas has a temperature lower than 15 000 K and a density higher than  $10.3 \text{ cm}^{-3}$ . Supernova feedback is implemented following the blast-wave formalism (Stinson, Seth & Katz 2006). Another stellar feedback mechanism ejects energy prior to supernova explosions, which accounts for the photoionizing radiation of massive stars (Stinson et al. 2013a). The free parameters in the feedback scheme were chosen such that a Milky Way–mass galaxy fits the stellar mass–halo mass relation at  $z = 0$ . The NIHAO simulations form the right amount of stars and cold gas as evidenced by the consistency with the stellar mass versus halo mass relations from abundance matching since  $z = 4$  (Wang et al. 2015) and the cold gas versus stellar mass relation at  $z = 0$  (Stinson, Dutton & Wang 2015).

## 2.2 Bulge–disc decomposition

We decompose our simulated galaxies at  $z = 0$  into disc and bulge components. We perform these decompositions considering only the star particles inside the spherical region within 20 per cent of the virial radius, with the centre of the halo being placed at the centre of mass of the target galaxy. We orient the axes such that the  $z$ -axis is parallel to the direction of the angular momentum vector of the galaxies. We do not identify and remove particles that might belong to a stellar halo as most of the stars within this radius actually belong to the disc–bulge system and decomposition results are not sensitive to the halo stars.

Many methods have been presented to perform bulge–disc decompositions in observed and simulated data sets. Importantly, these methods correspond to different definitions of a ‘bulge’ and hence it is important to pick the definition and then the method most adequate for the questions to be answered. To illustrate the importance of choosing a method, we first compare two standard but very distinct methods: a kinematic method based on the particle orbits and a photometric method based on the surface density.

Kinematic decompositions of stellar systems have evolved over the last decade. Abadi, Navarro & Steinmetz (2003) introduced a one-dimensional decomposition based on the circularity parameter of stellar orbits. The circularity parameter  $\varepsilon$  is defined as  $j_z/j_c$ , where  $j_z$  is the  $z$ -component of the AM vector of a stellar particle when the galactic disc lies on the  $x$ – $y$  plane, and  $j_c$  is the norm of the specific AM vector of a hypothetical particle at the same location on a circular orbit. In this work, we define  $j_c = \sqrt{GM}r$ , where  $r$  is the radius of the particle. The higher the circularity, the more the particle’s motion corresponds to a disc-like orbit. The kinematic method does a good job determining the relative mass of the disc and spheroid (see also Scannapieco et al. 2011; Martig et al. 2012). It assumes that the spheroid is non-rotating and thus has a symmetric

distribution of circularities around  $\varepsilon \sim 0$ . The thin disc gives the sharp peak at circularities close to  $\varepsilon \sim 1$ . We identify the spheroidal component by this assumption so that its mass is  $M_{\text{spheroid}} = 2 \times M(\varepsilon < 0)$ .

Secondly, we decompose galaxies into discs and bulges photo-metrically following the observational approach of Obreschkow & Glazebrook (2014). We generate a face-on image of the stellar component and extract one-dimensional stellar surface density profiles for each galaxy. Explicitly, we bin the particles by their cylindrical radii and divide the mass in each bin by the surface area of the annulus. The stellar surface density profiles hence obtained are then fitted by an exponential function

$$\Sigma_d(r) = \Sigma_{d,0} \exp\left(-\frac{r}{R_d}\right), \quad (1)$$

where  $R_d$  is the scale radius of the profile and  $\Sigma_{d,0}$  is the central surface density. We determine these two parameters with a least-squares minimization, excluding the inner half-mass radius to avoid fitting the exponential to the bulge.

Using the disc fits, we then identify the bulge stars. To do so, we bin the galaxy into 100 radial bins, each corresponding to an annulus in the face-on projection. In each annulus  $i$ , the mass fraction  $f_i$  of the stars in the bulge is calculated by

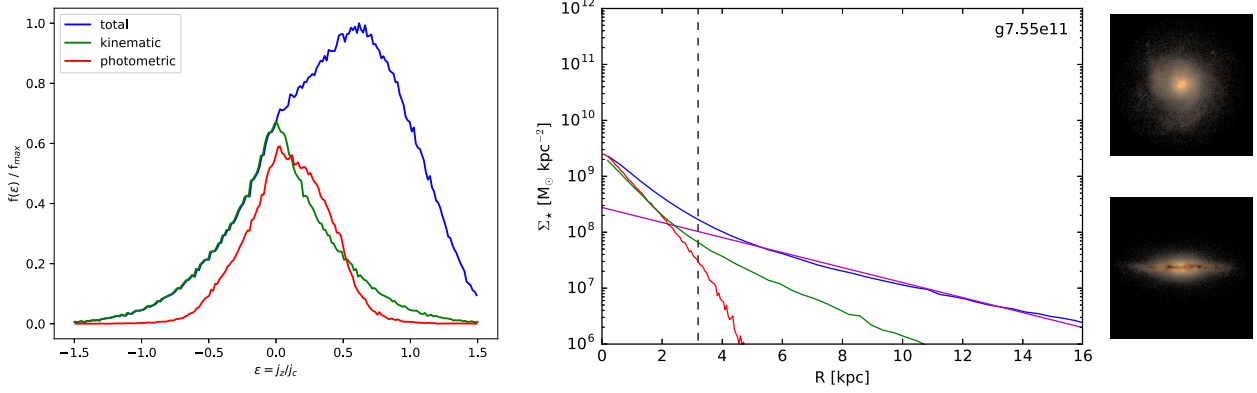
$$f_i = \frac{\Sigma_{\text{total},i} - \Sigma_{d,i}}{\Sigma_{\text{total},i}}, \quad (2)$$

where  $\Sigma_{\text{total},i}$  is the mean stellar surface density in the annulus and  $\Sigma_{d,i}$  is the disc surface density of the fit  $\Sigma_d(r)$ , evaluated at the central radius of the annulus. This definition of  $f_i$  is only adopted out to the radius, where the total surface density first falls below  $\Sigma_d(r)$ . Beyond this radius, we set  $f_i = 0$  to avoid including spiral arms and halo stars in the bulge mass. The global  $B/T$  is then defined as  $B/T = M_*^{-1} \sum_i f_i m_i$ , where  $m_i$  is the total stellar mass in the annulus  $i$  and  $M_*$  is the total stellar mass in the galaxy.

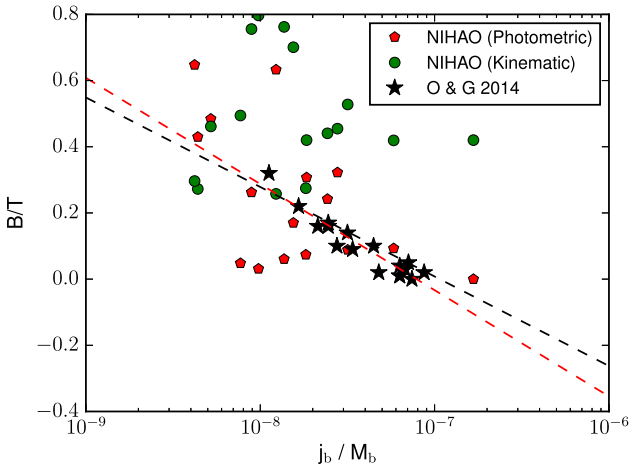
We use the kinematic criterion to decide which of the star particles in each annulus are bulge star particles. We therefore label, in each annulus  $i$ , the particles with the lowest circularities as bulge star particles, until they make up a mass fraction  $f_i$ . An illustration of the bulge particles identified in this way is shown in Fig. 6 (coloured points and yellow stars), discussed later.

Fig. 1 shows both the kinematic and photometric decompositions of the galaxy g7.55e11. The kinematic decomposition relies on the circularity distribution shown in the left-hand panel: By definition, the negative part of this distribution and a mirrored positive part (green line) are said to be the ‘kinematic bulge’. In turn, the ‘photometric bulge’ is identified as the excess above an exponential surface density profile (red line in the right-hand panel). The circularity distribution and surface densities of all stars are shown as blue lines in both panels, while the kinematic and photometric bulges are shown as green and red lines, respectively. The rightmost small panels show the face-on and edge-on views of the galaxy after processing it through the radiative transfer code SUNRISE (Jonsson 2006). In this discy galaxy the circularity distributions of the kinematic and photometric bulges are similar. However, their surface density profiles differ significantly. In fact, the kinematically identified bulge extends to almost three half-mass radii, which is difficult to reconcile with the standard conception of bulges but instructive in that it shows that pressure support is relevant even at such large scales. Most other galaxies show more disparity between the kinematic and photometric decompositions (see Fig. B3).

Fig. 2 shows a comparison between simulated galaxies from our sample that have bulges decomposed kinematically (green) and



**Figure 1.** Left: the distribution of the circularity parameter  $\varepsilon$  for all stellar particles within five half-mass radii of galaxy g7.55e11 (blue line), bulge particles selected by kinematic decomposition (green line), and bulge particles selected by photometric decomposition (red line). Right: stellar surface density profiles of same galaxy (blue filled circle) at  $z = 0$ . The magenta line shows the exponential fit of the disc component and the dashed line shows the half-mass radius. The images illustrate the face-on and edge-on synthetic images of the galaxies after processing them via the Monte Carlo radiative transfer code SUNRISE (Jonsson 2006). All images measure 50 kpc on a side.



**Figure 2.** Representation of the simulated galaxies and THINGS observations (Obreschkow & Glazebrook 2014) in the  $(j_b/M_b, B/T)$  plane. The red and black dashed lines are linear fits to both data sets.

photometrically (red) and those in Obreschkow & Glazebrook (2014) adopting a natural 2D projection of the  $M_b$ - $j_b$ - $B/T$  correlation that approximately minimizes the scatter. The baryons in the galaxies are defined as the total mass of the stars and the cold gas ( $T < 10^4$  K) within  $0.2R_{\text{vir}}$ . The specific AM vector of these baryons is calculated as

$$\mathbf{j}_b = \frac{|\sum m_i \mathbf{r}_i \times \mathbf{v}_i|}{\sum m_i}, \quad (3)$$

where  $\mathbf{r}_i$  are the distance vectors from the centre of mass and  $\mathbf{v}_i$  are the velocities in the the centre-of-mass frame. The linear fits shown as red (corresponding to photometric decomposition) and black lines (corresponding to THINGS observations) show a good agreement. However, the NIHAO galaxies with photometric decomposition yield a larger scatter than the observations, which may be attributed to the observational selection of regular gas-rich field galaxies. The NIHAO galaxies with kinematic decomposition are clearly offset, and show much less correlation between  $B/T$  and  $j_b/M_b$ . The Pearson correlation coefficient of galaxies with photometric decomposition is  $-0.50$ , while that of galaxies with kinematic decomposition amounts to an insignificant  $+0.06$ .

This discrepancy mainly comes from the difference in the decomposition methods. As described above, the kinematic bulges have a symmetric circularity distribution and are hence non-rotating, on average. However, the empirical relation between  $B/T$  and  $j_b/M_b$  (stars in Fig. 2) relies on photometrically identified bulges, which turn out to be mostly ‘pseudo-bulges’ (Obreschkow & Glazebrook 2014) that can have some rotational support. Therefore, it is no surprise that the photometric  $B/T$  matches the THINGS observations better than the kinematic  $B/T$ .

A priori, there is no objective definition of bulges, and different definitions are used for different purposes in the literature (Kormendy 1977; Kautsch et al. 2006; Lackner & Gunn 2012; Fabricius, Coccato & Bender 2014). The purpose of this work is to explore the ‘bulges’ defined as central overdensities, i.e. the photometric  $B/T$  values. It is likely that this photometric definition of bulges picks out a large number of pseudo-bulges, which make up the majority of the bulges in spiral galaxies in the local Universe (Fisher & Drory 2011). Although such pseudo-bulges are often described as subsystems of galactic discs, it is by no means trivial to understand how these bulges evolve and why their mass correlates with global disc properties – the topics that we will focus on in the remainder of this paper. Henceforth, ‘bulge’ will refer to the photometrically identified bulge, whether it has classical or pseudo-bulge-like properties.

### 2.3 $j$ - $M$ distribution

In this section, we analyse the NIHAO galaxies to determine the specific AM  $j_b$  contained in their baryons at  $z = 0$ , in order to compare the scaling relation between  $M_b$  and  $j_b$  to observations.

In Fig. 3, our results are plotted against observed galaxies from the THINGS and LITTLE THINGS analyses (Obreschkow & Glazebrook 2014; Butler et al. 2017). The location of the simulated galaxies on the diagram is similar to the observed sample. The points in Fig. 3 are colour-coded according to the  $B/T$ , which we deliberately calculated in an analogous way to the observations, as described in section 2.2. We perform the fits with the HYPERFIT package (Robotham & Obreschkow 2015). The best fit to the simulated galaxies has a slope ( $\alpha = 0.59 \pm 0.03$ ) similar to the simplistic analytical prediction of  $\alpha = 2/3$  (Fall 1983). The difference between simulations and observations might be accounted for by

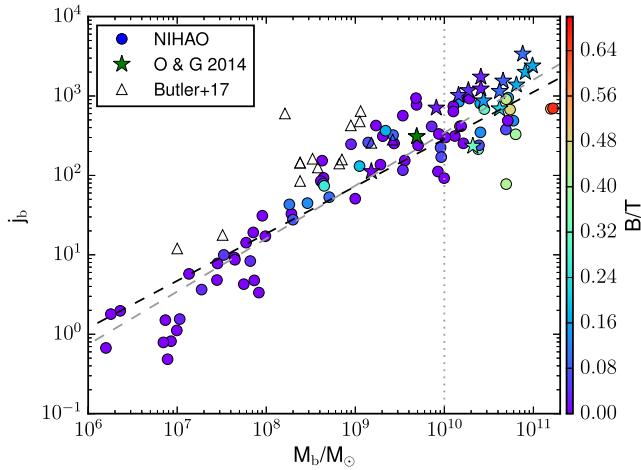


**Figure 3.** Specific AM–mass diagram ( $j_b - M_b$ ) for baryons of simulated galaxies, THINGS observations (Obreschko & Glazebrook 2014), and LITTLE THINGS observations (Butler, Obreschko & Oh 2017). The black dashed line is the best fit for simulated galaxies and the grey dashed line is the fitting with a fixed slope  $2/3$ .

the observational bias of selecting only H I-rich objects (especially for LITTLE THINGS) with small bulge components. We refer the reader to Wang, Obreschko & Lagos (2018), where we present a detailed analysis of the connection between gas fraction and angular momentum in NIHAO galaxies. The second reason can be that the simulations also include a small fraction of ionized gas in the cold gas, and they might slightly overestimate the observable baryon mass (Stinson et al. 2015; Sales et al. 2017). Last but not the least, El-Badry, Quataert & Wetzell (2018) studied a sample of zoom-in galaxies and compared the AM measured with the rotation curve of H I and simply vector-summing the AM. The comparison shows, for low-mass galaxies, that the approach that measures AM by the H I rotation curve overestimates galaxies’ stellar AM as those stars are primarily supported by dispersion. The discrepancy also consists with this argument.

Obreschko & Glazebrook (2014) found that the 16 regular spiral galaxies from the THINGS survey display a tight correlation between  $M_b$ ,  $j_b$ , and  $B/T$ . The lower specific AM of the simulated galaxies with higher bulge-to-total ratio is consistent with the empirical finding that the disc and bulge components lie roughly on parallel sequences on the  $j-M$  plane, separated by a factor of  $\sim 5$  in  $j$  (Fall & Romanowsky 2013). Fig. 4 compares the individual stellar components, bulge (upper panel) and disc (lower panel), in the  $j_*$ – $M_*$  diagram. The best-fitting lines for each component again show a slope similar to  $\alpha = 2/3$ , and the ratio of the specific AM between the discs and the bulges ranges from 4 to 10 across the 10 galaxies. The scatter in  $j_*$  is about 0.6 dex (standard deviation) for both components. The baryonic  $j-M$  diagram confirms that the simulated galaxies do not suffer from the overcooling problem or the AM catastrophe (Navarro & White 1994; Navarro & Steinmetz 2001) and can be regarded as good laboratories for in-depth studies of the AM evolution.

The main purpose of this work is to understand the origin of bulge stars in disc-dominated galaxies. To do so, we explicitly exclude bulge-dominated objects; i.e., we only retain galaxies with  $B/T < 0.5$ . Galaxies with baryon masses below  $10^{10} M_\odot$  often admit no bulges or these bulges are very small and hard to detect, also in the simulation. Such low-mass galaxies also tend to be cold-gas-dominated systems in which stellar mass scalings become more

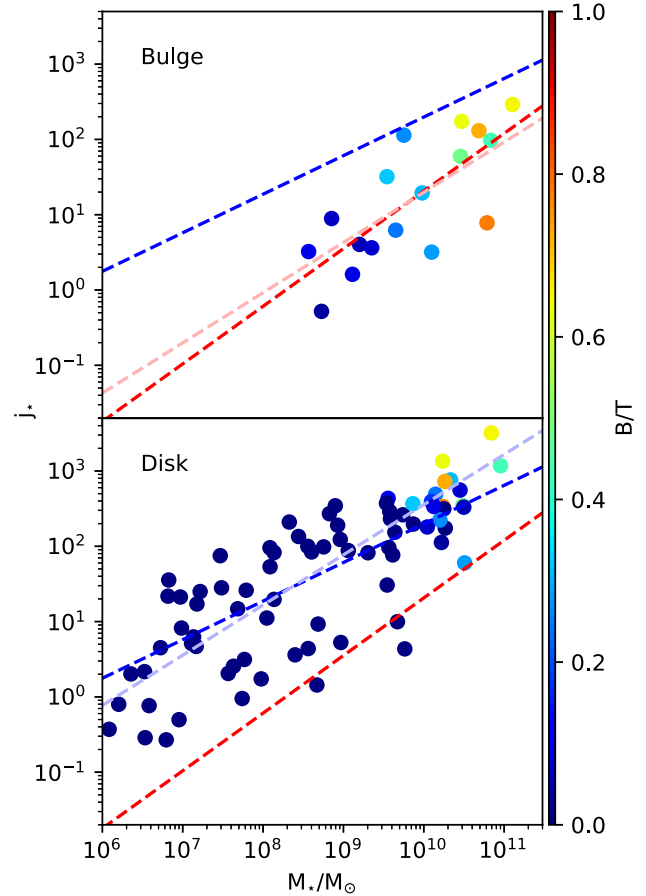


**Figure 4.** Representation of the simulated galaxies on the mass–AM plane, split into disc (lower panel) and bulge (upper panel) stars. The blue and red dashed lines are the best fits for the disc and bulge components, when using a free slope. The light-blue and light-red dashed lines are corresponding fits with a fixed  $2/3$  slope. The points are colour-coded by  $B/T$ .

scattered. We therefore chose to limit the analysis to galaxies with  $M_b > 10^{10} M_\odot$ . The resulting sample contains 10 galaxies.

## 2.4 Bulge properties

In Fig. 5, the upper panel shows  $V/\sigma$  versus ellipticity  $\varepsilon$  of the bulge stars at  $z = 0$  for each galaxy. The rotational velocity  $V$  is the mass-weighted mean of the tangential velocities (i.e. in the plane of the disc). The velocity dispersion  $\sigma$  is the mass-weighted mean of  $(v_R^2 + v_z^2)$ , where  $v_R$  is the cylindrical radial velocity (in the plane) and  $v_z$  is the vertical (parallel to the rotation axis). The ellipticities are calculated as  $\varepsilon = 1 - \lambda_{\min}/\lambda_{\text{mean}}$ , where  $\lambda_{\min}$  is the minimum eigenvalue of a bulge’s moment of inertia tensor and  $\lambda_{\text{mean}}$  is the mean of the other two eigenvalues. Fig. 5 shows a positive correlation between  $V/\sigma$  and  $\varepsilon$ , meaning that more rotation-supported bulges tend to be flatter. These quantities also correlate with  $B/T$ , in the sense that larger bulge mass fractions correspond to flatter and more rotation-supported bulges. The maximum ellipticity in the sample is around 0.4, which is still quite spherical (axes ratio about 0.6). This galaxy (g1.92e12) has an extended central overdensity which contains amounts of particles with  $\varepsilon \sim 1$  so that the  $V/\sigma$  of this bulge can be more than 0.80.

The lower panel in Fig. 5 shows the specific star formation rate (sSFR) of the bulge as a function of the bulge mass. In the

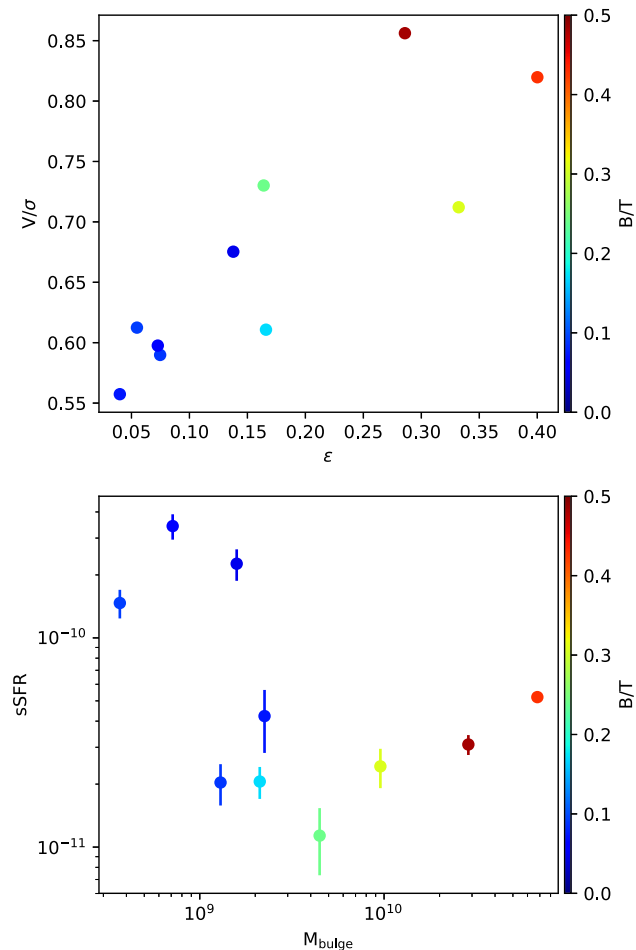


**Figure 5.** The relative dynamic importance of rotation ( $V/\sigma$ ) as a function of ellipticity for all bulge stars of each galaxy at  $z = 0$  (upper panel) and specific star formation rates as a function of bulge mass (lower panel). The points are colour-coded by  $B/T$ . The error bars in the lower panel represent the shot noise of specific star formation rates for each galaxy.

simulations, star formation rates are calculated as the total stellar mass formed in the last 100 Myr, divided by that time interval. On average, the specific star formation rates of bulges in disc-dominated galaxies are  $\sim 5 \times 10^{-11} \text{ yr}^{-1}$ . The four low-mass bulges that have a high specific star formation rate are star-forming bulges, although their low mass also increases the specific star formation. These 10 bulges span from passive bulges ( $\log \text{ sSFR} < -10.5 \text{ Gyr}^{-1}$ ) to active bulges ( $\log \text{ sSFR} < -10.0 \text{ Gyr}^{-1}$ ); the threshold of the sSFR is suggested by Fisher & Drory (2010). The sSFRs of the bulges are independent of their ellipticities. The two plots in Fig. 5 illustrate the diversity of bulges in the NIHAO sample.

## 2.5 Convergence radius

The minimum radius above which the results of a simulation are not significantly affected by the finite resolution is crucial in the numerical study of bulges. Although running higher resolution simulations is a way to determine the numerical convergence, it would be extremely expensive for a simulation suite. A common criterion for convergence has been suggested by Power, Navarro & Frenk (2003) for collisionless simulations, based on the two-body relaxation time-scale for particles in a gravitational potential. This criterion ensures that the mean density inside the convergence radius is

within 10 per cent of the converged value obtained in a simulation of much higher resolution.

Tollet, Macciò & Dutton (2015) study the cusp or core of dark matter density profiles with the NIHAO suite. They find that this convergence radius, normalized to virial radius, is quite constant for all NIHAO galaxies, as all NIHAO galaxies have similar numbers of particles. At  $z = 0$ , this convergence radius is 0.4–0.7 per cent of the  $R_{\text{vir}}$ , which is comparable with the mean radial distance of the bulge star particles at  $z = 0$ . However, as noticed by Schaller, Frenk & Bower (2015), this convergence criterion is too restrictive as it applies to pure DM simulations. As the magnitude of the differences between the profiles from hydrodynamical simulations and pure DM simulations is significantly larger than 10 per cent, the criterion can be relaxed to the 20 per cent level. Since we study the stars in the bulge region, where star particles dominate, the convergence radii should be smaller than in Tollet et al. (2015). Following the prescription of Schaller et al. (2015), the convergence radius for the sample in this work derived by star particles is of the order of 0.08–0.1 per cent of the  $R_{\text{vir}}$  ( $\sim 100 \text{ pc}$ ) and the typical bulge size is of the order of 1 kpc, i.e. about an order of magnitude larger, so the majority of bulge star particles are comfortably above this resolution limit. The range of the convergence radii is shown in Fig. 9 as a grey bar, compared with the radial distribution of bulge stellar particles at redshift  $z = 0$ . Also note that the convergence radii decrease as the redshift increases. Hence, we expect the migration processes of bulge stars not to be significantly impacted by numerical resolution effects.

## 2.6 Tracking bulge particles across time

SPH simulations have the advantage that particles can be easily tracked across time. Therefore, we can determine the dynamic history of each stellar particle that ends in the bulge at  $z = 0$ . Each particle has one specific identifier (id), which can link every dark matter, gas, and star particle to its progenitor through the whole simulation. Each gas particle may form several (up to 3) star particles. When a new star particle forms from a gas particle, a linker id is created to keep track of the gas particle that produced this particular star particle.

Due to the relatively large time interval of  $\sim 200 \text{ Myr}$  between snapshots, we cannot determine the exact location and velocity when the star particles form from gas particles. When a star particle first appears, it has already moved for a certain time (0–200 Myr). Therefore, we also keep track of the location and velocity of the corresponding star-forming gas particle in the previous snapshot. This gas particle, which will have formed a new star particle in the immediate next snapshot, is here called a ‘parent gas particle’. It is difficult to interpolate from a parent gas particle to a new star particle given that the time interval of  $\sim 200 \text{ Myr}$  is comparable to a dynamical time. In future work, we aim to overcome this limitation through the use of 8 times more outputs (simulations in progress).

## 3 FORMATION OF BULGE

### 3.1 Original location of bulge stars

Let us now explore where the bulge stars at  $z = 0$  formed at higher redshifts in our sample of 10 simulated late-type galaxies. We distinguish three regions of origin, shown in Fig. 6: (1) the ‘galaxy’, defined by a cylinder (white dashed rectangle) of radius  $R_{\text{cyn}} = 5r_e$  and height  $h_{\text{cyn}} = r_e$ , where  $r_e$  is the redshift-dependent half-mass radius of galaxy; (2) the ‘halo’, defined as the region outside the

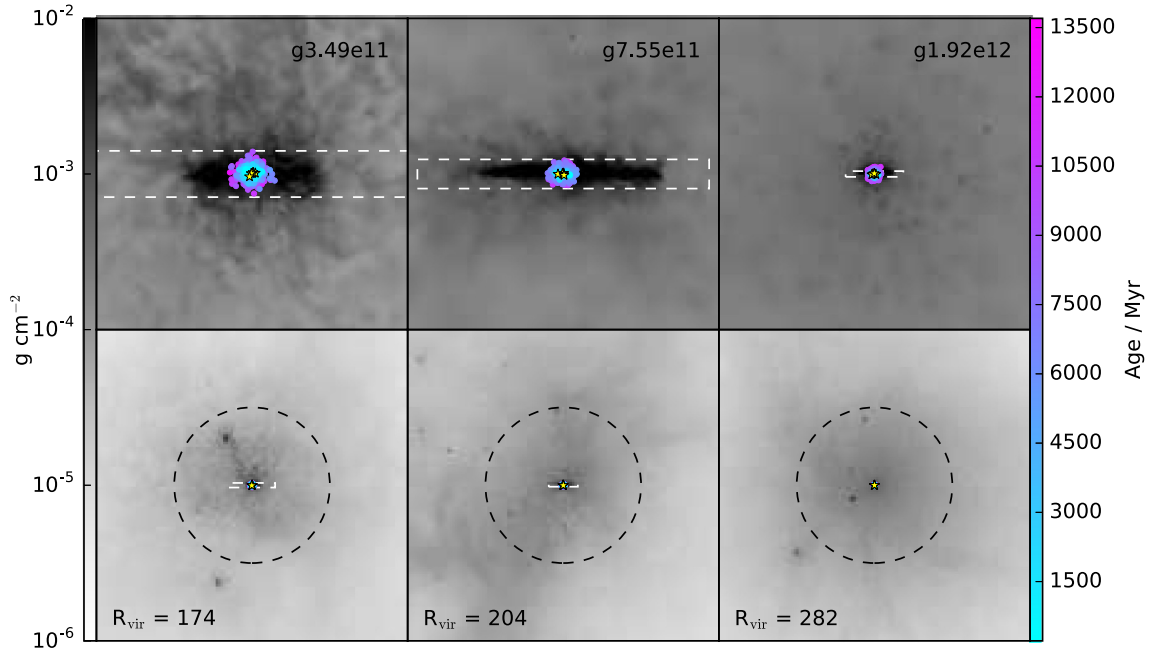


**Figure 6.** Column density map of gas at  $z = 0$ . The size of the upper panels is 40 percent of the virial radius at one side and the size of the lower panels is 10 times larger than the upper panels. The dashed circles are the virial radius and the dashed rectangles are defined as the galaxy region. The points are star particles colour-coded by their ages and the yellow stars are newly formed star particles that formed between the last two snapshots of the simulations.

galaxy, but inside the virial radius (black dashed circle) at the given redshift; (3) the ‘environment’, defined as the region outside the halo. Processes in the ‘halo’ or the ‘environment’ are often called *ex situ* processes in the literature. In principle, it is possible to subdivide the galaxy region in the aim of separating stars formed in a central star burst from stars formed in a disc. However, we found this division to be cumbersome at higher redshifts, especially at cosmic times when the disc is hardly stable and thick (high pressure support), which are indeed the cosmic times where most stars formed. We therefore avoid labelling stars as bulge or disc stars when they form, but instead quantify the star formation dynamics inside the galaxy by tackling the radius, velocity, and AM evolution of every star that lands in the bulge at  $z = 0$ .

The fractions of bulge stars formed in each region are shown in Fig. 7 as a function of the final  $B/T$ . These fractions rely on the location of the parent gas particles (solid line) and newly formed star particles (dashed line) in the following snapshot (i.e.  $\sim 200$  Myr later), since we have no information about the exact location of the star formation in between snapshots. The fractions calculated by the parent gas particles show that the majority (about 75 per cent) of them have already settled in the galaxy region when they form stars. Most of the remaining bulge stars (20 per cent of all bulge stars) were formed in the halo, leaving no more than a few per cent of bulge stars to form outside the halo. In other words, mergers do not play an important role in the bulge formation in our sample.

When measuring these fractions using the newly formed stars instead of the parent gas particles, the picture looks somewhat different. We still find that most of the bulge stars ( $> 95$  per cent) form inside the virial radius. However, the balance between halo and galaxy is different: Even more bulge stars (95 per cent on average) now appear to originate from the galaxy. This difference suggests that most parent gas particles inside the halo convert into stars as soon as they reach the galactic disc – an explanation that is in line with the higher density and thus lesser stability and increased self-shielding expected in the galaxy.

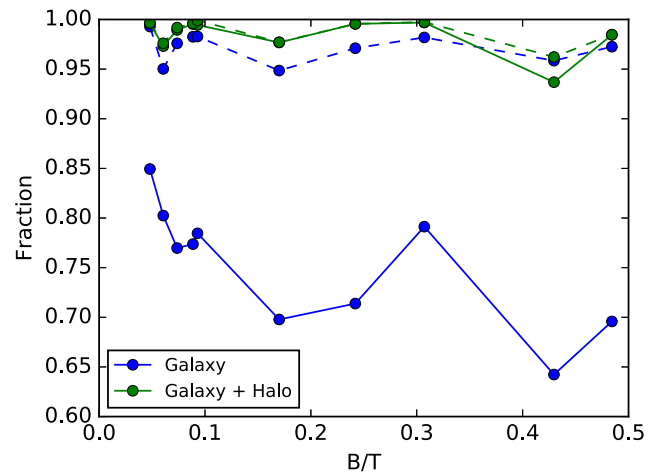


**Figure 7.** Accumulated mass fraction of bulge stars formed in the galaxy region (blue) and in the virial radius (green). Solid lines show the fraction calculated by gas parent particles and dashed lines show the fraction calculated by newly formed star particles. The green dashed line is nearly identical to the green solid line.

### 3.2 Evolution of AM of bulge stars

The stars in bulges are always the low-AM component of the galaxies, even in the case of rotationally supported bulges, due to their small radius relative to the disc. As discussed before, most of the bulge stars (95 per cent) of the galaxies in our simulation formed inside the galaxy. One scenario for this bulge formation in the galaxy is that cold gas in the disc forms stars with high AM and the stars then lose their AM by dynamical friction to migrate into the bulge region. The other possibility is that the cold gas first dissipates its AM and then forms stars with low AM in or close to the central region. The probability distribution function of the specific AM  $j$  can

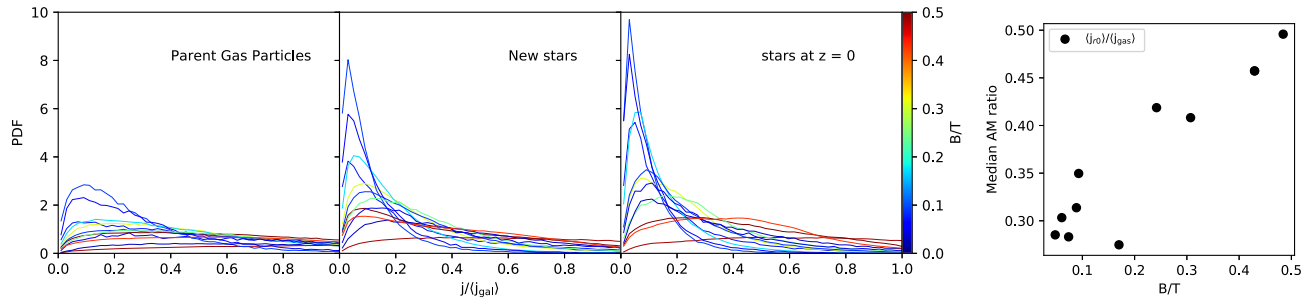


**Figure 8.** Left: normalized distribution of specific AM of parent gas particles (left), newly formed bulge star particles (middle), and bulge stellar particles at  $z = 0$  (right). The curves are colour-coded by the bulge-to-total ratio. Right: the median of the specific angular momentum ratio between bulge star particles at  $z = 0$  ( $j_{r0}$ ) and parent gas particles ( $j_{\text{gas}}$ ).

be used to clarify the scenario and provide useful insights regarding the details of bulge formation.

The left-hand panel of Fig. 8 shows the distribution of  $j$  of the parent gas particles (left), newly formed bulge star particles (middle), and bulge star particles at  $z = 0$  (right) for each simulation. The specific AM is normalized by the mean specific AM ( $j_{\text{gal}}$ ) of all particles (stars, gas, and dark matter) within 20 per cent of the virial radius at  $z = 0$ . Each solid curve represents a galaxy and the curves are coloured by their  $B/T$  value. Qualitatively, the curves with different  $B/T$  have significantly different shapes and evolution features. For the galaxies with higher  $B/T$ , the initial distributions of parent gas particles have a lower peak and longer tails compared to the galaxies with lower bulge fractions. For newly formed bulge stars and  $z = 0$  bulge stars, the peaks of the distributions move inwards, which means that the stars lose their AM during the processes of forming the bulge. However, the distributions of galaxies with lower  $B/T$  have much smaller widths and higher peaks than those of the galaxies with higher  $B/T$ . A similar trend is found in observations of spiral galaxies (Sweet, Fisher & Glazebrook 2018).

The right-hand panel of Fig. 8 shows the median of the specific AM ratio between bulge star particles at  $z = 0$  and parent gas particles. A ratio of unity would mean that the  $j$  of bulge stars is conserved from (just before) their formation to  $z = 0$ , while smaller ratios indicate a loss of  $j$ . The plot shows a clear trend for a higher loss in  $j$  in the case of smaller bulge final fractions  $B/T$ . The specific AM ratio between bulge star particles at  $z = 0$  and newly formed stars (rather than star-forming gas) shows a similar trend with the bulge fraction  $B/T$ , but the mean ratio is higher ( $\sim 80$  per cent). In the following section, the implications of the loss in  $j$  on the stellar dynamics will be discussed in more detail.

### 3.3 Evolution of locations and velocities of bulge stars

According to the definition of the specific AM  $j$ , a variation in  $j$  of the bulge stars can come from a variation of the orbital radius or the orbital velocity.

We compute the distributions of the orbital radii and velocities of the parent gas particles, newly formed star particles, and bulge star particles at  $z = 0$ , in analogy to the  $j$  distributions in Fig. 8. In Fig. 9, the upper panel shows the normalized distributions of the radial distance and the vertical distance, in a coordinate system, whose orientation is fixed to that of the final snapshot at  $z = 0$ . The distances are normalized to the virial radius at  $z = 0$ . The general trend is that both the radial and vertical distance decrease with time; i.e., the bulge stars migrate inwards. In contrast to the  $j$  distributions, these distance distributions have an almost universal shape with no

clear trend as a function of  $B/T$ . Two galaxies (red and light-blue lines in the upper panel of Fig. 9) have a substantial fraction of bulge stars formed outside the virial radius and there is no statistically significant relation with the galaxies'  $B/T$ . It is necessary to note that the vertical distance of most parent gas particles is smaller than their radial distance shown by the distributions. This means that the migrations of the bulge particles are not isotropic, and they are preferentially near the disc plane during the migration.

The lower panel in Fig. 9 shows the normalized distribution of the azimuthal and vertical velocity. The distributions and their variations have a clear dependence on the galaxies' morphology. The distributions of azimuthal velocities (solid lines) and their variations for the galaxies with lower  $B/T$  ( $< 10$  per cent) are similar to the  $j$  distributions shown in Fig. 8 (a). In particular, the mean velocities decrease with time and the width of the distributions gets narrower. At higher  $B/T$ , the distributions of azimuthal velocities show a different trend. The peaks of the distributions for the parent gas particles are lower and the shapes of the distributions are wider than those of the distributions of galaxies with lower  $B/T$ . The particle velocities generally decrease in the panels for the newly formed star particles and bulge star particles at  $z = 0$ . Fig. 10 highlights the main trends of Fig. 9. Interestingly, as long as the  $B/T > 20$  per cent, the median of the velocity of the bulge stars actually increases from the time these stars form to  $z = 0$ . Their  $z$ -component of the velocity is negligible compared with their azimuthal velocity.

## 4 DISCUSSION

### 4.1 Linking the evolution of specific angular momentum, velocity, and distance

In the left-hand panel of Fig. 8, we tackled the evolution of bulge star particles from their parent gas particle phase to the final stage at  $z = 0$ . The specific AM mainly decreases in the parent gas phase, immediately ( $< 200$  Myr) before the stars form: As the cooling gas reaches the disc region, it dissipates the AM by fluid viscosity and dynamical friction. Once the stars have formed, they are no longer subject to viscosity, and hence the AM loss continues at a much lower rate, set purely by gravitational torques. Globally, we find that more AM is dissipated for smaller final bulge fractions, as shown in the right-hand panel of Fig. 8.

Given this loss of AM, we can then attempt to explain the change in the radius and velocity distributions (Figs 9 and 10). In a Keplerian framework, the circular velocity at a given radius is set by the enclosed mass, which is  $v = \sqrt{GM(r)/r}$  for spherical mass distributions. Hence, the balance between change in radius and velocity

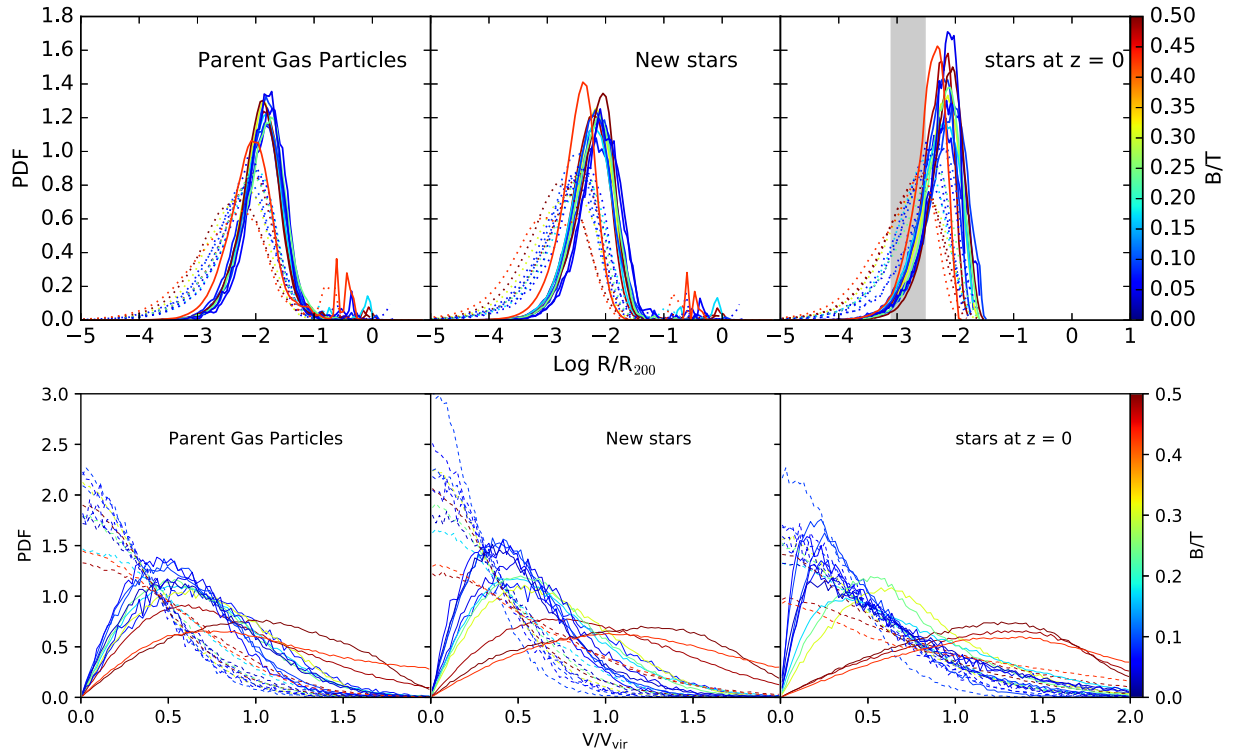


**Figure 9.** Upper panel: normalized distribution of radial distance (solid line) and height (dotted line) with fixed  $z$ -direction. The left-hand panel is for the parent gas particles, the middle panel is for the newly formed bulge stars, and the right-hand panel is for the bulge stars at  $z = 0$ . The grey vertical region shows the range of convergence radii. Lower panel: normalized distribution of azimuthal velocity (solid line) and  $z$  component of velocity (dotted line) with fixed  $z$ -direction. The left-hand panel is for the parent gas particles, the middle panel is for the newly formed bulge stars, and the right-hand panel is for the bulge stars at  $z = 0$ . The curves are colour-coded by the  $B/T$ .

depends on this mass, which itself depends on the bulge mass. For small bulge masses ( $B/T < 0.1$ ), the specific AM reduction is paralleled by a decrease in radius and velocity. However, for higher bulge masses, this AM reduction is achieved by a loss in radius under increase in velocity. The circular velocity simply has to increase due to the deeper potential caused by the bulge itself. This is apparent in Fig. 11, which shows the rotation curves, measured by the median circular velocity (solid lines) and the enclosed mass (dashed lines) for different  $B/T$ . The rotation curves exhibit qualitatively different shapes for small and large  $B/T$ , with larger values leading to more peaked rotation curves.

#### 4.2 Bulge formation by migration?

The global star formation density in the Universe peaks around  $z = 1 \sim 3$  (Hopkins & Beacom 2006). In this epoch, star-forming galaxies were more ‘clumpy’ than in the local Universe (Abraham, Tanvir & Santiago 1996; Conselice, Bershady & Jangren 2000; Elmegreen et al. 2005). The migration of bulge stars towards the centre is normally discussed at the level of clumps. One scenario argues clumps have lifetimes long enough to allow them to migrate inwards forming the galaxy bulge (Bournaud, Perret & Renaud 2014; Forbes et al. 2014). This would predict that clumps closer to the galaxy centre are older, which is indeed suggested by observations (Lamberti et al., 2018, submitted). Alternatively, older clumps may be closer to the galaxy centre as a result of inside-out formation of the disc (Murray, Quataert & Thompson 2010; Genel, Naab & Genzel 2012). Fig. 12 shows the normalized age distributions of the bulge star particles of each galaxy at  $z = 0$ . Most bulges are dominated by

old stars (formed at  $z > 1$ ), and only two galaxies with very small  $B/T$  host young bulges. Guedes et al. (2013) and Okamoto (2013) found similar results; i.e., the bulk of the pseudo-bulge stars forms quickly at high redshift by a combination of non-axisymmetric disc instabilities and tidal interactions or mergers. They concluded that the main formation mechanism of pseudo-bulges are high-redshift starbursts, rather than secular evolution of galactic discs.

To investigate the migration of bulge stars, we here take a different approach: We do not explicitly consider clumps or distinguish between star formation in the disc and bulge, but instead focus directly on the change in radius of the population of bulge stars at  $z = 0$ . The reason is that the resolution of the simulations is insufficient to define the clumpy structure. This is because clumps have shown to have sizes from dozens of pc to a kpc (Livermore, Jones & Richard 2015). We found that the majority of the bulge is contributed by stars formed in the ‘galaxy’, i.e. in the disc + bulge region, mainly around less than 1 percent  $R_{\text{vir}}$ . By comparing the distribution of radial and vertical distances (solid and dotted lines in Fig. 8, top), we find that most of this star formation took place in an oblate region, akin to a thick disc. From there, the radii of the stellar orbits decrease, on average, by a factor 2.5, for all  $B/T$  values. While the present simulations do not have the time resolution to tackle spiralling orbits of clumps, the global change in radius nonetheless argues for a migration scenario similar to that of Bournaud et al. (2014). Similar simulations with 8 times more snapshots are in preparation. In the future, we plan to work on distinguishing inner and outer disc origin for bulge stars throughout cosmic time and connect this to the AM build-up of the bulge.

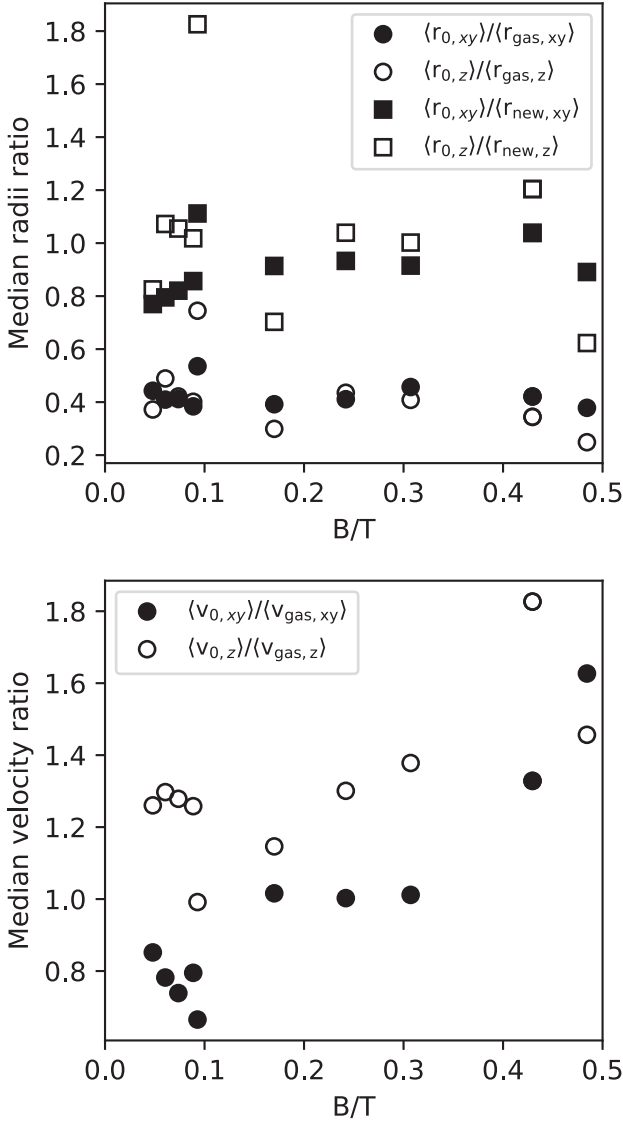


**Figure 10.** Upper panel: median ratio of radial distance and height between parent gas particles and bulge star particles at  $z = 0$ . The squares show the median ratio between newly formed star particles and bulge star particles at  $z = 0$ . Lower panel: median ratio of azimuthal velocity (black points) and vertical velocity (white points) between parent gas particles and bulge star particles at  $z = 0$ .

### 4.3 AM evolution as a function of $B/T$

In Fig. 8 (right), the AM loss of bulge stars from their formation to  $z = 0$  appears to be negatively correlated with the final bulge fraction  $B/T$ . This is an important result, which calls for a physical explanation. A plausible scenario is that both the AM loss and the final bulge fraction correlate with the spin parameter  $\lambda \propto j/M^{2/3}$  (Peebles 1969) of the stellar system. Let us consider each of these correlations separately.

Fig. 4 shows that bulges and discs in the simulations approximately reproduce the respective empirical  $j$ - $M$  relation of field galaxies. Empirically, classical bulges, pseudo-bulges, and elliptical galaxies all fall on roughly the same power-law relation of slope  $2/3$  (Fall & Romanowsky 2018). In other words, all these systems have a universal stellar  $\lambda$ . If we take this empirical fact for granted, bulge stars that form with a higher  $\lambda$  value are thus bound to loose

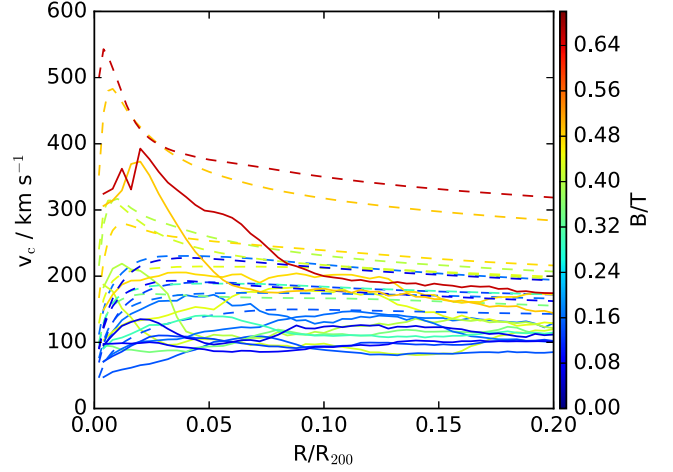


**Figure 11.** Rotation curves of the median rotation velocity (solid line) and spherically circular velocity  $\sqrt{GM/r}$  (dashed line) colour-coded with the  $B/T$  ratio.

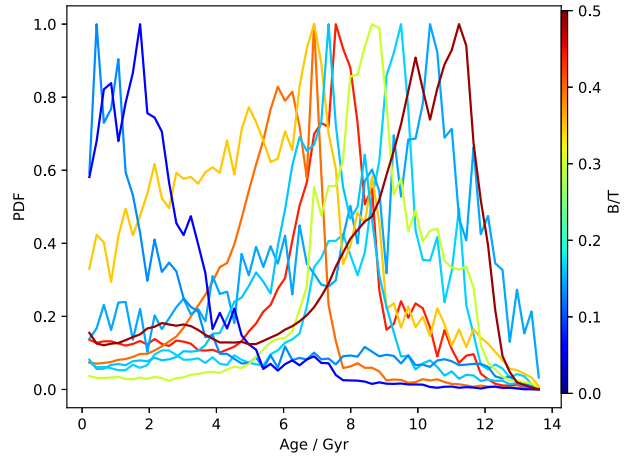


**Figure 12.** Normalized age distribution of the bulge star particles for the NIHAO galaxies analysed in this paper. The colour of the lines indicates the  $B/T$  ratio, as labelled by the colourbar.

more AM. Hence,  $\lambda$  and the AM loss are positively correlated. Recently, Lagos, Schaye & Bahé (2018b) analysed a large sample of simulated galaxies by combining the EAGLE and Hydrangea (cluster) simulations (Schaye et al. 2015; Bahé, Barnes & Dalla Vecchia 2017). They explicitly explored the relation between the stellar and halo spin parameters and found a positive correlation. Galaxy mergers tend to wash out that correlation, which means that galaxies in the absence of mergers follow the halo  $j$  closely (see also Zavala et al. 2016).

On the other hand, Fig. 13 shows the relation between  $j/M^{2/3}$  of all the parent gas particles and the bulge fraction  $B/T$ . Clearly, gas with a higher spin parameter forms a smaller bulge, similarly to empirical models that find that galaxies with a lower stellar or baryonic  $j/M^{2/3}$  value exhibit more significant bulges (Romanowsky & Fall 2012; Obreschkow & Glazebrook 2014; Fall & Romanowsky 2018; Posti et al. 2018; Sweet et al. 2018). While this relation is theoretically not yet fully understood, it is likely a consequence of global (bar-mode) or local (Toomre) instabilities scaling roughly as  $j/M^{2/3}$  (Obreschkow & Glazebrook 2014).

Having established that higher  $\lambda$  values (of star-forming gas or newly formed stars) lead to less bulge formation as well as to more

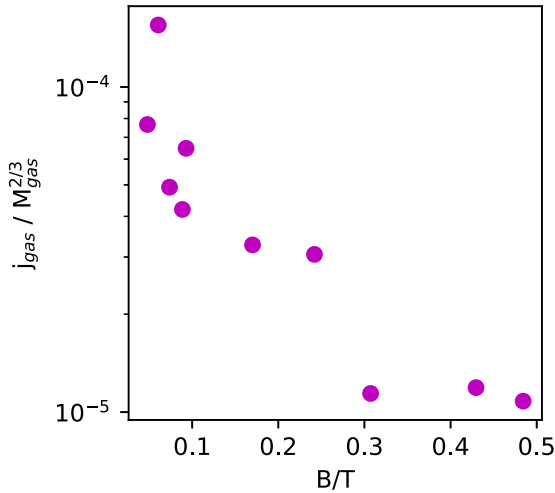


**Figure 13.** The  $j/M^{2/3}$  of the parent gas particles as the function of the bulge fraction  $B/T$ .

AM loss when forming a bulge means that the AM loss of bulge stars must be negatively correlated with the final bulge mass fraction. In other words, the AM ratio between the parent gas of bulge stars and bulge stars at  $z = 0$  correlates *positively* with the final bulge fraction  $B/T$ , explaining Fig. 8 (right).

## 5 CONCLUSIONS

In this paper, we analysed the dynamic evolution of stars that end up in the central bulge of disc-dominated galaxies at  $z = 0$ , using a sample of 10 galaxies from the NIHAO simulation. The ‘bulge’ is defined as all the excess mass above an exponential disc in the central region of galaxies, dominated by rotation-supported pseudo-bulges. The simulated galaxies lie on a similar  $j_{\text{bar}}-M_{\text{bar}}$  relation as observed star-forming spiral galaxies in the local Universe. Furthermore, the galaxies with large  $B/T$  have lower  $j_{\text{bar}}$  values, also in relatively good agreement with modern (interferometric) observations. These observational verifications justify the use of this sample of simulated galaxies to investigate the formation and AM evolution of bulge stars. Our results can be summarized as follows.

(i) By tracking bulge star particles back in time to their parent gas particles, we found that  $\gtrsim 95$  per cent of the stellar mass in bulges at  $z = 0$  formed *in situ* in the galaxy, while about  $\sim 3$  per cent of the mass stems from star formation outside the galaxy but inside the virial radius (i.e. in satellites). A small and comparable mass fraction of the bulge stars formed outside of the virial radius in the simulated sample.

(ii) The AM evolution of the bulge stars, from their formation to  $z = 0$ , shows a clear correlation with the final  $B/T$  value of the galaxy: The lower the final  $B/T$  value, the more AM is dissipated away from the bulge stars (Fig. 8, right).

(iii) On average, bulge stars move towards the galaxy centre by about a factor 2, *irrespective* of the final  $B/T$ . By contrast, the circular velocity of the bulge stars tends to slightly increase with time, and this increase scales with the final  $B/T$  value.

The specific AM  $j$ , mass  $M$ , and bulge-to-total ratio  $B/T$  obey a strong correlation in regular galaxies (Romanowsky & Fall 2012), even within the subset of gas-rich star-forming spirals (Obreschkow & Glazebrook 2014). The bulges decomposed photometrically means the central overdensity components, this raises

the question of how and whether this bulge mass is driven by the AM in the galaxy. Our analysis showed that the AM history of bulge stars in this definition correlates with the galaxy’s final  $B/T$ . Qualitatively, galaxies with higher AM (at fixed mass), and hence a requirement to dissipate more AM to move stars to the centre, tend to form smaller bulges. The details of this connection remain, however, clouded by the limited spatial and temporal resolution in the simulations. By increasing the number of snapshots for one simulation in the NIHAO sample, we will soon have the ability to rebuild the trajectories of bulge stars from their formation to  $z = 0$  in 10 times more detail.

## ACKNOWLEDGEMENTS

We are grateful to Pascal Elahi, Matthieu Schaller, and Jiang Chang for helpful comments and discussions. We also thanks the anonymous referee for a constructive report that helped improve the clarity of the paper. The analysis was performed using the PYNBODY package (<http://pynbody.github.io>), which was written by Andrew Pontzen and Rok Roškar in addition to the authors. This research was supported by Australia Research Council Discovery Project 160102235. This research was carried out on the High Performance Computing resources at New York University Abu Dhabi; on the THEO cluster of the Max-Planck-Institut für Astronomie and on the HYDRA clusters at the Rechenzentrum in Garching. CL is funded by a Discovery Early Career Researcher Award (DE150100618) and by the ARC Centre of Excellence for All Sky Astrophysics in 3 Dimensions (ASTRO 3D). XK acknowledges the support from NSFC project No.11333008 and 973 program No. 2015CB857003.

## REFERENCES

- Abadi M. G., Navarro J. F., Steinmetz M., Eke V. R., 2003, *ApJ*, 597, 21  
 Abraham R. G., Tanvir N. R., Santiago B. X., Ellis R. S., Glazebrook K., van den Bergh S., 1996, *MNRAS*, 279, L47  
 Agertz O., Teyssier R., Moore B., 2011, *MNRAS*, 410, 1391  
 Aumer M., White S. D. M., Naab T., Scannapieco C., 2013, *MNRAS*, 434, 3142  
 Bahé Y., Barnes D.J., Dalla Vecchia C., 2017, *MNRAS*, 470, 4186B  
 Binney J., Gerhard O., Silk J., 2001, *MNRAS*, 321, 471  
 Bournaud F., Perret V., Renaud F. et al., 2014, *ApJ*, 780, 57B  
 Brook C. B. et al., 2011, *MNRAS*, 415, 1051  
 Brook C. B., Stinson G., Gibson B. K., Wadsley J., Quinn T., 2012, *MNRAS*, 424, 1275  
 Bullock J. S., Dekel A., Kolatt T. S., Kravtsov A. V., Klypin A. A., Porciani C., Primack J. R., 2001, *ApJ*, 555, 240  
 Butler K. M., Obreschkow D., Oh S., 2017, *ApJ*, 834, L4  
 Christensen C. R., Brooks A. M., Fisher D. B., Governato F., McCleary J., Quinn T. R., Shen S., Wadsley J., 2014, *MNRAS*, 440L, 51  
 Colín P., Avila-Reese V., Roca-Fàbrega S., Valenuela O., 2016, *ApJ*, 829, 98  
 Conselice C. J., Bershady M. A., Jangren A., 2000, *ApJ*, 529, 886  
 Cortese L. et al., 2016, *MNRAS*, 463, 170  
 D’Onghia E., Navarro J. F., 2007, *MNRAS*, 380L, 58  
 D’Onghia E., Burkert A., Murante G., Khochfar S., 2006, *MNRAS*, 372, 1525  
 Davies R. L., Illingworth G., 1983, *ApJ*, 266, 516  
 DeFelippis D., Genel S., Bryan G., Fall S. M., 2017, *ApJ*, 841, 16  
 Dutton A. A., Macciò A. V., 2014, *MNRAS*, 441, 3359  
 Dutton A. A. et al., 2017, *MNRAS*, 467, 493  
 El-Badry K. et al., 2018, *MNRAS*, 473, 1930  
 Elmegreen D. M., Elmegreen B. G., Rubin D. S., Schaffer M. A., 2005, *ApJ*, 631, 85  
 Fabricius M. H. et al., 2014, *MNRAS*, 441, 2212

- Fall S. M., 1983, Proc. IAU Symp. 100, Internal Kinematics and Dynamics of Galaxies. D. Reidel Publishing Co., Dordrecht, 391
- Fall S. M., Efstathiou G., 1980, *MNRAS*, 193, 189
- Fall S. M., Romanowsky A. J., 2013, *ApJ*, 796L, 26
- Fall S. M., Romanowsky A. J., 2018, preprint ([arXiv:1808.02525](https://arxiv.org/abs/1808.02525))
- Fisher D. B., Drory N., 2010, *ApJ*, 716, 942
- Fisher D. B., Drory N., 2011, *ApJ*, 733, L47
- Forbes J. C., Krumholz M. R., Burkert A., Dekel A., 2014, *MNRAS*, 438, 1552
- Genel S. et al., 2012, *ApJ*, 745, 11
- Genel S. et al., 2015, *ApJ*, 804, 40
- Governato F., Willman B., Mayer L., Brooks A., Stinson G., Valenzuela O., Wadsley J., Quinn T., 2007, *MNRAS*, 374, 1479
- Grand R. J. J. et al., 2017, *MNRAS*, 467, 179
- Guedes J., Callegari S., Madau P., Mayer L., 2011, *ApJ*, 742, 76
- Guedes J., Mayer L., Carollo M., Madau P., 2013, *ApJ*, 772, 36
- Gutcke T. A., Stinson G. S., Macciò A. V., Wang L., Dutton A. A., 2017, *MNRAS*, 464, 2796
- Hopkins P. F., Beacom J. F., 2006, *ApJ*, 651, 142
- Hopkins P. F., Cox T. J., Younger J. D., Herquist L., 2009, *ApJ*, 691, 1168
- Jonsson P., 2006, *MNRAS*, 372, 2
- Kannan R., et al., 2014, *MNRAS*, 437, 2882
- Kannan R., Macciò A. V., Fontanot F., Moster B. P., Karman W., Somerville R. S., 2015, *MNRAS*, 452, 434
- Kautsch S. J., Grebel E. K., Barazza F. D., Gallagher J. S., III, 2006, *A&A*, 445, 765
- Keller B. W., Wadsley J., Benincasa S. M., Couchman H. M. P., 2014, *MNRAS*, 442, 3013
- Kormendy J., 1977, *ApJ*, 218, 333
- Kormendy J., Kennicutt R. C., 2004, *ARA&A*, 42, 603
- Lackner C. N., Gunn J. E., 2012, *MNRAS*, 421, 2277
- Lagos C. P. et al., 2017, *MNRAS*, 464, 3850
- Lagos C. P. et al., 2018a, *MNRAS*, 473, 4956
- Lagos C. P., Schaye J., Bahé Y., Van de Sande J., Kay S. T., Barnes D., Davis T. A., Dalla Vecchia C., 2018b, *MNRAS*, 476, 4327
- Livermore R. C. et al., 2015, *MNRAS*, 450, 1812
- Marinacci F., Pakmor R., Springel V., 2014, *MNRAS*, 437, 1750
- Martig M., Bournaud F., Croton D. J., Dekel A., Teyssier R., 2012, *ApJ*, 756, 26
- Murante G. et al., 2015, *MNRAS*, 447, 178
- Murray N., Quataert E., Thompson T. A., 2010, *ApJ*, 709, 191
- Navarro J. F., Steinmetz M., 2001, *ApJ*, 528, 477
- Navarro J. F., White S. D. M., 1994, *MNRAS*, 267, 401
- Obreja A., Stinson G. S., Dutton A. A., Macciò A. V., Wang L., Kang X., 2016, *MNRAS*, 459, 467
- Obreschkow D., Glazebrook K., 2014, *ApJ*, 784, 26
- Okamoto T., 2013, *MNRAS*, 428, 718
- Peebles P. J. E., 1969, *ApJ*, 155, 393
- Piontek F., Steinmetz M., 2011, *MNRAS*, 410, 2625
- Planck Collaboration XVI, Ade P. A. R. Planck Collaboration XVI et al., 2014, *A&A*, 571, AA16
- Posti L., Pezzulli G., Fraternali F., Di Teodoro E. M., 2018, *MNRAS*, 475, 232
- Power C., Navarro J. P., Jenkins A., Frenk C. S., White S. D. M., Springel V., Stadel J., Quinn T., 2003, *MNRAS*, 338, 14
- Robertson B., Yoshida N., Springel V., Hernquist L., 2004, *ApJ*, 606, 32
- Robertson B. et al., 2006, *ApJ*, 645, 986
- Robotham A. S. G., Obreschkow D., 2015, *PASA*, 32, 33
- Romanowsky A. J., Fall S. M., 2012, *ApJS*, 203, 17
- Roškar R., Teyssier R., Agertz O., Wetzstein M., Moore B., 2014, *MNRAS*, 444, 2823
- Sales L. V. et al., 2017, *MNRAS*, 464, 2419
- Scannapieco C., White S. D. M., Springel V., Tissera P. B., 2009, *MNRAS*, 396, 696
- Scannapieco C., White S. D. M., Springel V., Tissera P. B., 2011, *MNRAS*, 417, 154
- Scannapieco C. et al., 2012, *MNRAS*, 423, 1726
- Schaller M. et al., 2015, *MNRAS*, 451, 1247
- Schaye J. et al., 2015, *MNRAS*, 446, 521
- Shen S., Wadsley J., Stinson G., 2010, *MNRAS*, 407, 1581
- Sokolowska A., Capelo P. R., Fall S. M., Mayer L., Shen S., Bonoli S., 2017, *ApJ*, 835, 289
- Springel V., Herquist L., 2005, *ApJ*, 622L, 9
- Stinson G. S., Seth A., Katz N., Wadsley J., Governato F., Quinn T., 2006, *MNRAS*, 373, 1074
- Stinson G. S., Bailin J., Couchman H., Wadsley J., Shen S., Nickerson S., Brook C., Quinn T., 2010, *MNRAS*, 408, 812
- Stinson G. S. et al., 2013, *MNRAS*, 436, 625
- Stinson G. S., Brook C., Macciò A. V., Wadsley J., Quinn T. R., Couchman H. M. P., 2013, *MNRAS*, 428, 129
- Stinson G. S. et al., 2015, *MNRAS*, 454, 1105
- Sweet S. M., Fisher D., Glazebrook K., Obreschkow D., Lagos C., Wang L., 2018, *ApJ*, 860, 37
- Teklu A. F., Remus R. S., Dolag K., Beck A. M., Burkert A., Schmidt A. S., Schulze F., Steinborn L. K., 2015, *ApJ*, 812, 29
- Tollet E. et al., 2015, *MNRAS*, 456, 3542
- van den Bosch F. C., 2001, *MNRAS*, 327, 1334
- van den Bosch F. C., Abel T., Rupert A. C., Hernquist L., White S. D. M., 2002, *MNRAS*, 576, 21
- Vogelsberger M. et al., 2014, *MNRAS*, 444, 1518
- Wadsley J. W., Stadel J., Quinn T., 2004, *New Astron.*, 9, 137
- Wadsley J. W., Veeravalli G., Couchman H. M. P., 2008, *MNRAS*, 387, 427
- Wang L., Dutton A. A., Stinson G. S., Macciò A. V., Penzo C., Kang X., Keller B. W., Wadsley J., 2015, *MNRAS*, 454, 83
- Wang L. et al., 2018, *ApJ*, 868
- Zavala J. et al., 2016, *MNRAS*, 460, 4466

**APPENDIX A: PARAMETERS**

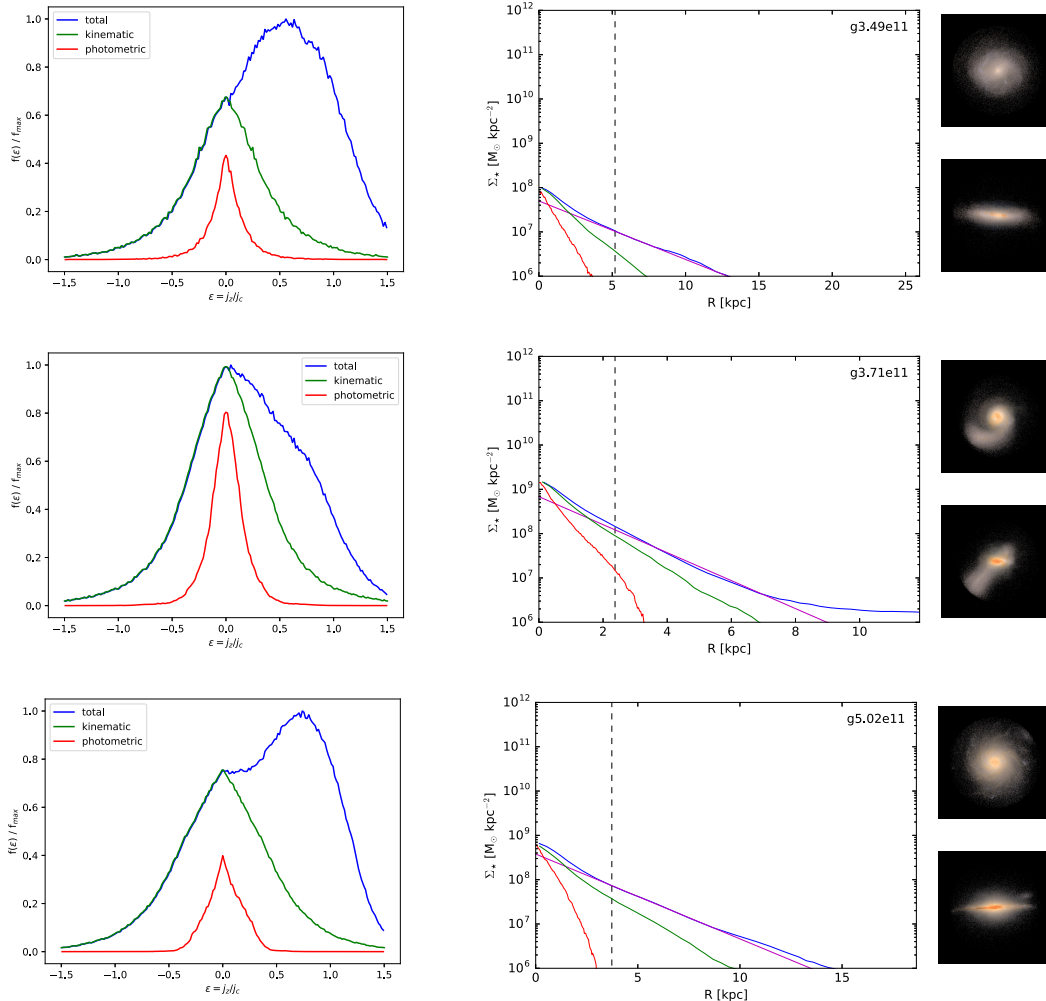
In this appendix, we summarize the bulge parameters of all galaxies at redshift  $z = 0$  through this paper. Table A1 contains the simulation ID, baryonic mass  $M_{\text{bar}}$ , baryonic specific angular momentum  $j_{\text{bar}}$ , photometric bulge-to-total ratio  $[B/T]_{\text{p}}$ , kinematic bulge-to-total ratio  $[B/T]_{\text{k}}$ , ellipticity  $\varepsilon$ ,  $V/\sigma$ , and specific star formation rate sSFR.

**Table A1.** Bulge parameters for galaxies at redshift  $z = 0$ .

Simulation ID	$M_{\text{bar}}$ $M_{\odot}$	$j_{\text{bar}}$ $\text{kpc km s}^{-1}$	$[B/T]_{\text{p}}$	$[B/T]_{\text{k}}$	$\varepsilon$	$V/\sigma$	sSFR $\text{yr}^{-1}$
g7.08e11	$5.22 \times 10^{10}$	$9.52 \times 10^2$	0.07	0.27	0.04	0.56	$4.23 \times 10^{-11}$
g7.55e11	$4.94 \times 10^{10}$	$9.11 \times 10^2$	0.31	0.42	0.33	0.71	$2.43 \times 10^{-11}$
g7.66e11	$6.32 \times 10^{10}$	$3.29 \times 10^2$	0.48	0.46	0.29	0.86	$3.09 \times 10^{-11}$
g3.49e11	$1.46 \times 10^{10}$	$8.49 \times 10^2$	0.09	0.42	0.05	0.61	$1.47 \times 10^{-10}$
g3.71e11	$1.64 \times 10^{10}$	$2.53 \times 10^2$	0.17	0.70	0.17	0.61	$2.06 \times 10^{-11}$
g5.02e11	$2.53 \times 10^{10}$	$8.03 \times 10^2$	0.09	0.53	0.07	0.59	$2.04 \times 10^{-11}$
g5.36e11	$2.54 \times 10^{10}$	$3.49 \times 10^2$	0.06	0.76	0.07	0.60	$3.42 \times 10^{-10}$
g5.38e11	$2.82 \times 10^{10}$	$6.84 \times 10^2$	0.24	0.44	0.16	0.73	$1.13 \times 10^{-11}$
g6.96e11	$4.91 \times 10^{10}$	$3.78 \times 10^2$	0.05	0.49	0.14	0.68	$2.26 \times 10^{-10}$
g1.92e12	$1.57 \times 10^{11}$	$6.89 \times 10^2$	0.43	0.27	0.40	0.82	$5.21 \times 10^{-11}$

**APPENDIX B: STELLAR SURFACE DENSITY PROFILES FOR INDIVIDUAL GALAXIES**

In this appendix, we present the circularity distribution of the total star particles and bulge components decomposed by kinematic and photometric methods, stellar surface density profiles, the exponential fit for disc components, and synthetic images of the galaxies.


**Figure B1.** Same as Fig. 1, but for galaxies g3.49e11, g3.71e11, and g5.02e11.

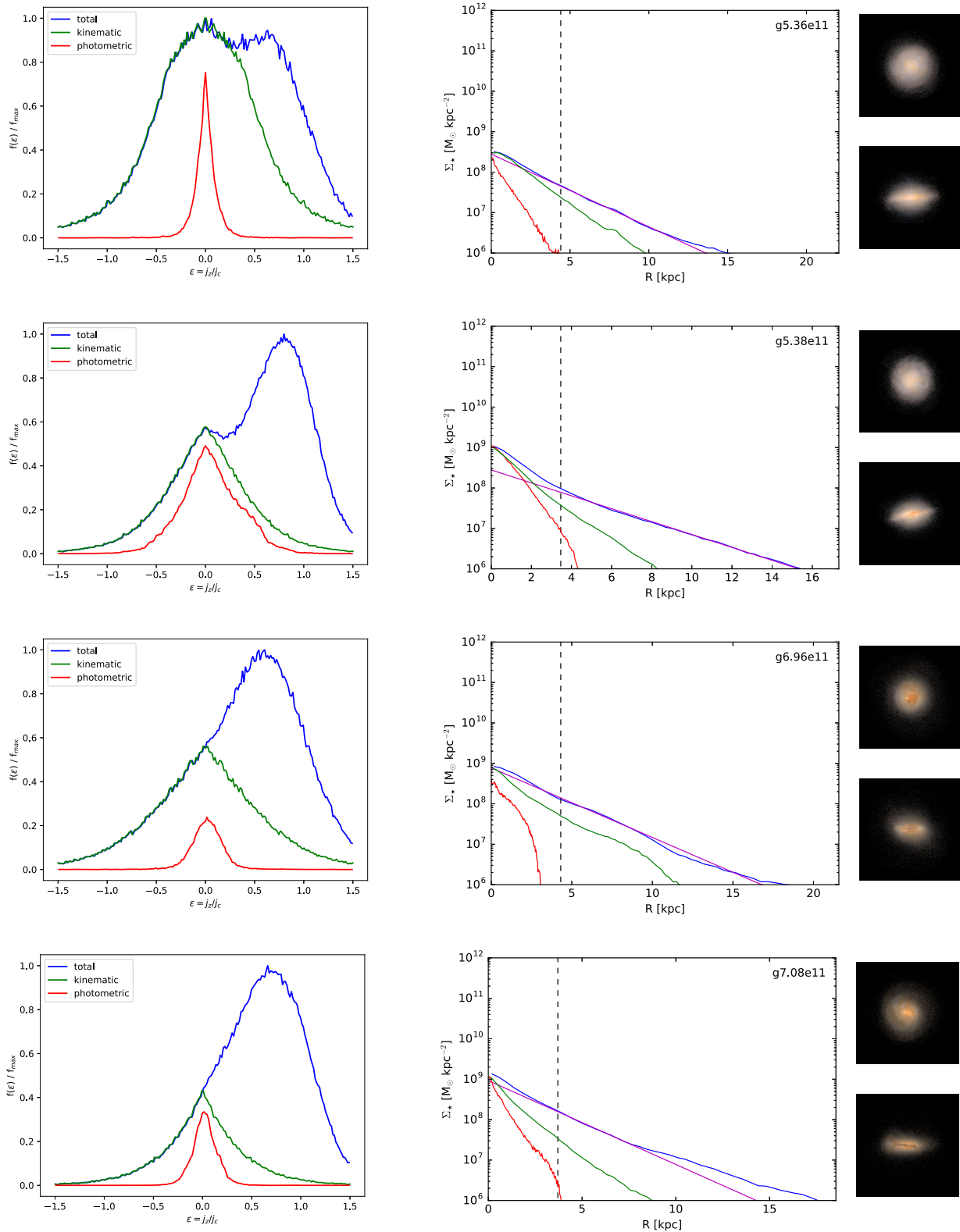


**Figure B2.** Same as Fig. 1, but for galaxies g5.36e11, g5.38e11, g6.96e11, and g7.08e11.

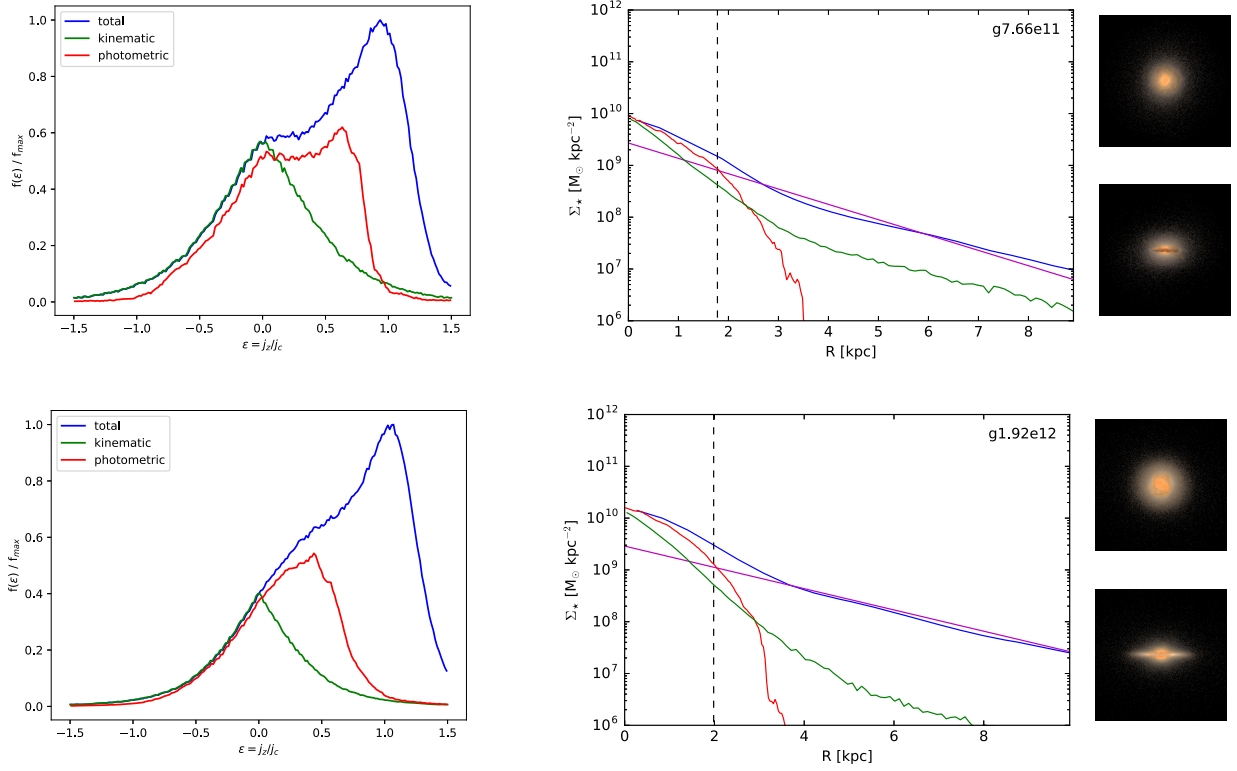


**Figure B3.** Same as Fig. 1, but for galaxies g7.66e11 and g1.92e12.

This paper has been typeset from a  $\text{\TeX}/\text{\LaTeX}$  file prepared by the author.